Performance Analysis of Oriented Feature Detectors

Fábio J. Ayres and Rangaraj M. Rangayyan
Department of Electrical and Computer Engineering,
University of Calgary, Calgary, Alberta, Canada T2N 1N4

Abstract

Oriented feature detectors are fundamental tools in image understanding, as many images display relevant information in the form of oriented features. Several oriented feature detectors have been developed; some of the important families of oriented feature detectors are steerable filters and Gabor filters. In this work, a performance analysis is presented of the following oriented feature detectors: the Gaussian second-derivative steerable filter, the quadrature-pair Gaussian second-derivative steerable filter, the real Gabor filter, the complex Gabor filter, and a line operator that has been shown to outperform the Gaussian second-derivative steerable filter in the detection of linear structures in mammograms. The detectors are assessed in terms of their capability to detect the presence of oriented features, as well as their accuracy in the estimation of the angle of the oriented features present in the image. It is shown that the Gabor filters yield the best detection performance and angular accuracy, whereas the steerable filters have the best performance in terms of computational speed.

1. Detection of oriented features

The presence of oriented features in images often conveys important information about the scene or the objects contained; the analysis of oriented patterns is an important task in the general framework of image understanding. Applications of oriented feature analysis include the analysis of satellite images [1], cereal grain inspection [2], fingerprint recognition [3], counting of asbestos fibers [4], and mammographic image analysis [5, 6, 7, 8].

The detection of oriented features is often influenced by the characteristic width of the feature under investigation, and the presence of noise. Individual oriented features are associated with a particular spatial width, such as the width of a spicule in a mammographic image, or that of a road seen in an aerial image. Hence, the ability of a technique to detect oriented features often depends on the proper calibration of some scale parameter that regulates the intrinsic width of the oriented feature detector, according to the width of the oriented feature of interest. Noise is another factor that may impair the performance of an oriented feature detector, because noise can mask the presence of oriented structures and may form spurious oriented structures in the image.

The purpose of the present work is to compare the detection performance and orientation accuracy of five selected oriented feature detectors: the Gaussian second-derivative steerable filter [9], the quadrature-pair Gaussian second-derivative steerable filter [9], the real Gabor filter [10], the complex Gabor filter [10], and the line operator of Dixon and Taylor [4]. The detection performance is defined in terms of the ability of each filter to detect linear structures in the presence of noise and imprecision in the specification of scale. The orientation accuracy is given in terms of the cumulative angle error for the pixels belonging to the oriented features in a test pattern.

1.1. Steerable filters

The concept of steerable filters was presented by Freeman and Adelson [9]. Steerable filters are a class of filters with the "steering property": the impulse response of a filter, rotated at an arbitrary angle, can be synthesized from a linear combination of rotated versions of the same filter's impulse response, for a set of pre-specified rotation parameters. Let $f(x,y)$ be the filter's impulse response, and $f_\theta(x,y)$ be the rotated impulse response at an angle θ. The steering property can be written as

$$f_\theta(x,y) = \sum_{j=1}^{M} k_j(\theta) f_{\theta_j}(x,y),$$

where θ_j is the jth basis angle, $j \in 1, 2, \cdots, M$, and $k_j(\theta)$ is the jth interpolating function.

1.1.1. Gaussian-derivative-based steerable filters. The partial derivatives of the Gaussian function provide a family of steerable filters [9]. In particular, the second derivative of the Gaussian has been used as a detector of linear structures in mammograms [7]. In this work, we implemented the second derivative of the Gaussian as follows:

$$s(x,y) = \frac{0.9213\,(2x^2 - 1)}{\sigma\sqrt{2}} \exp\left(-\frac{x^2 + y^2}{2\sigma^2}\right),$$

where σ determines the scale of the filter. The integral of $|s(x,y)|^2$ over the $\mathbb{R}^2$ plane is normalized to unity. This function requires three basis angles to implement the steering property: $\theta_1^s = 0$, $\theta_2^s = \pi/3$, and $\theta_3^s = 2\pi/3$. Then, the steering property can be written as

$$s_\theta(x,y) = \sum_{j=1}^{3} k_j^s(\theta)\, s_{\theta_j^s}(x,y),$$

where $s_\theta(x,y)$ denotes $s(x,y)$ rotated by an angle θ, and the interpolating functions $k_j^s(\theta)$ are given by

$$k_j^s(\theta) = \frac{1}{3}\left[1 + 2\cos(2(\theta - \theta_j^s))\right].$$

Let $I(x,y)$ be the given image, and $W_\theta^s(x,y)$ be the result of filtering $I(x,y)$ with the filter $s_\theta(x,y)$, for a given value of θ. The squared magnitude function $|W_\theta^s(x,y)|^2$ is periodic in θ; hence, it can be decomposed into a Fourier series. Only even frequencies appear in the series as a consequence of the squaring operation. Let $C_1^s(x,y)$ and $C_2^s(x,y)$ be the cosine and sine coefficients of the second harmonic of $|W_\theta^s(x,y)|^2$. Then, the local orientation $\phi^s(x,y)$ of $I(x,y)$ is defined as $\phi^s(x,y) = \theta_{opt}^s(x,y) + \pi/2$, where

$$
\begin{aligned}
\theta_{opt}^s(x,y) &= \frac{1}{2}\arctan\left(\frac{C_2^s}{C_1^s}\right) \\
&= \frac{1}{2}\arctan\left(\frac{\sqrt{3}(W_{\pi/3}^s - W_{2\pi/3}^s)}{W_{\pi/3}^s + W_{2\pi/3}^s - 2W_0^s}\right).
\end{aligned}
$$

The coordinates (x,y) have been dropped for clarity. The magnitude component of the orientation field is given by $E^s(x,y) = |W_{\theta_{opt}}^s(x,y)|$. The magnitude $E^s(x,y)$ and the local orientation $\phi^s(x,y)$ compose the orientation field extracted with the steerable Gaussian second-derivative filter.

1.1.2. Quadrature-pair Gaussian-derivative-based steerable filters. The Gaussian second-derivative steerable filter forms a quadrature pair with its Hilbert transform. Freeman and Adelson [9] present an approximation $s^h(x,y)$ of the Hilbert-transformed filter composed of a polynomial times a Gaussian function in (x,y). With the inclusion of the scale factor σ, the Hilbert-transformed steerable kernel implemented in our work is as follows:

$$s^h(x,y) = \frac{-2.205x + 0.9780x^3}{\sigma\sqrt{2}} \exp\left(-\frac{x^2 + y^2}{2\sigma^2}\right).$$

The integral of $|s^h(x,y)|^2$ over the $\mathbb{R}^2$ plane is normalized to unity. This function requires four basis angles to steer: $\theta_1^h = 0$, $\theta_2^h = \pi/4$, $\theta_3^h = \pi/2$, and $\theta_4^h = 3\pi/4$. The corresponding interpolation functions are given by

$$k_j^h(\theta) = \frac{1}{2}\left[\cos(\theta - \theta_j^h) + \cos(3(\theta - \theta_j^h))\right].$$

Analogous to the steerable Gaussian second-derivative filter in the preceding section, we define $W_\theta^h(x,y)$ as the output of filtering the given image $I(x,y)$ with the filter $s_\theta^h(x,y)$. The combined energy of the quadrature pair is given by $|W_\theta^{sh}(x,y)|^2 = |W_\theta^s(x,y)|^2 + |W_\theta^h(x,y)|^2$, which can be decomposed in a Fourier series of only even frequencies in θ, for a given (x,y). Let C_1^{sh} and C_2^{sh} be the cosine and sine coefficients of the second harmonic of $|W_\theta^{sh}(x,y)|^2$. Then, the local orientation $\phi^{sh}(x,y)$ of $I(x,y)$ is defined as $\phi^{sh}(x,y) = \theta_{opt}^{sh}(x,y) + \pi/2$, where

$$\theta_{opt}^{sh}(x,y) = \frac{1}{2}\arctan\left(\frac{C_2^{sh}}{C_1^{sh}}\right)$$

and

$$
\begin{aligned}
C_1^{sh} =\ & \frac{4}{9}(W_0^s)^2 + \frac{2}{9}W_0^s W_{\pi/3}^s + \frac{2}{9}W_0^s W_{2\pi/3}^s - \frac{2}{9}(W_{\pi/3}^s)^2 \\
& - \frac{4}{9}W_{\pi/3}^s W_{2\pi/3}^s - \frac{2}{9}(W_{2\pi/3}^s)^2 + \frac{3}{8}(W_0^h)^2 \\
& + \frac{1}{8}\sqrt{2}W_0^h W_{\pi/4}^h - \frac{1}{8}\sqrt{2}W_0^h W_{3\pi/4}^h - \frac{1}{8}\sqrt{2}W_{\pi/4}^h W_{\pi/2}^h \\
& + \frac{1}{4}W_{\pi/4}^h W_{3\pi/4}^h - \frac{3}{8}(W_{\pi/2}^h) - \frac{1}{8}\sqrt{2}W_{\pi/2}^h W_{3\pi/4}^h \\
C_2^{sh} =\ & \frac{2}{9}\sqrt{3}W_0^s W_{\pi/3}^s - \frac{2}{9}\sqrt{3}W_0^s W_{2\pi/3}^s + \frac{2}{9}\sqrt{3}(W_{\pi/3}^s)^2 \\
& - \frac{2}{9}\sqrt{3}(W_{2\pi/3}^s)^2 + \frac{1}{8}\sqrt{2}W_0^h W_{\pi/4}^h - \frac{1}{4}W_0^h W_{\pi/2}^h \\
& + \frac{1}{8}\sqrt{2}W_0^h W_{3\pi/4}^h + \frac{3}{8}(W_{\pi/4}^h)^2 + \frac{1}{8}\sqrt{2}W_{\pi/4}^h W_{\pi/2}^h \\
& - \frac{1}{8}\sqrt{2}W_{\pi/2}^h W_{3\pi/4}^h - \frac{3}{8}(W_{3\pi/4}^h)^2 .
\end{aligned}
$$

The coordinates (x,y) have been dropped for clarity. The magnitude of the output of the quadrature-pair filter is given by $E^{sh}(x,y) = |W_{\theta_{opt}}^{sh}(x,y)|$. The magnitude $E^{sh}(x,y)$ and the local orientation $\phi^{sh}(x,y)$ compose the orientation field extracted with the steerable quadrature-pair Gaussian second-derivative filter.

The Gaussian second-derivative filter will be henceforth referred to as the steerable filter only; the quadrature-pair Gaussian second-derivative filter will be referred to as the quadrature steerable filter.

1.2. Gabor filters

Gabor filters are a category of filters obtained from the modulation of a sinusoidal function (real or complex) by a Gaussian envelope [10]. The Gabor filter represents the best compromise between spatial localization and frequency localization, as measured by the product between the spatial extent and the frequency bandwidth of the filter [10]. In image processing applications, Gabor filters may be used as oriented feature detectors [11, 5, 6].

1.2.1. The real Gabor filter . The real Gabor filter kernel oriented at the angle $\theta = -\pi/2$ is given by

$$g^r(x,y) = \frac{1}{2\pi\sigma_x\sigma_y}\exp\left[-\frac{1}{2}\left(\frac{x^2}{\sigma_x^2}+\frac{y^2}{\sigma_y^2}\right)\right]\cos(2\pi fx).\tag{1}$$

Kernels at other angles can be obtained by rotating this kernel over the range $[-\pi/2,\pi/2]$. In the present work, the parameters in Equation (1), namely σ_x, σ_y, and f, are derived from design rules as follows:

- Let τ be the full-width at half-maximum of the Gaussian term in Equation (1) along the x axis. Then, $\sigma_x = \tau/(2\sqrt{2\ln 2}) = \tau/2.35$.

- The cosine term has a period of τ; therefore, $f = 1/\tau$.

- The value of σ_y is defined as $\sigma_y = l\,\sigma_x$, where l determines the elongation of the Gabor filter in the y direction, as compared to the extent of the filter in the x direction. In this work, we use $l = 8$.

The parameter τ controls the scale of the filter.

Let $\phi^r(x,y)$ be the angle of the oriented feature at (x,y), and $g_k^r(x,y)$, $k = 0,1,\cdots,17$, be the real Gabor filter oriented at $\alpha_k = -\pi/2 + \pi k/18$. The functions $g_k^r(x,y)$, $k = 0,1,\cdots,17$ form a bank of real Gabor filters, from which the orientation field can be extracted. Let $I(x,y)$ be the image being processed, and $W_k^r(x,y) = (I * g_k^r)(x,y)$ represent the Gabor-filtered images, where the asterisk denotes linear convolution. Then, the orientation field of $I(x,y)$ produced by the bank of real Gabor filters is given by the angle

$$\phi^r(x,y) = \alpha_{k_{\max}} \text{ where } k_{\max} = \arg\{\max_k[|W_k^r(x,y)|]\},$$

and by the magnitude of the output of the real Gabor filter at the optimal orientation $E^r(x,y) = |W_{k_{\max}}^r(x,y)|$.

1.2.2. The complex Gabor filter. The complex Gabor filter kernel oriented at the angle $\theta = -\pi/2$ is given by

$$\begin{aligned}g^c(x,y) &= \frac{1}{2\pi\sigma_x\sigma_y}\exp\left[-\frac{1}{2}\left(\frac{x^2}{\sigma_x^2}+\frac{y^2}{\sigma_y^2}\right)\right]\exp(j2\pi fx)\\ &= g^r(x,y)+jg^i(x,y),\end{aligned}\tag{2}$$

where $g^r(x,y)$ is the real Gabor filter of the preceding section, and $g^i(x,y)$ is the imaginary component of the complex Gabor filter, given by

$$g^i(x,y) = \frac{1}{2\pi\sigma_x\sigma_y}\exp\left[-\frac{1}{2}\left(\frac{x^2}{\sigma_x^2}+\frac{y^2}{\sigma_y^2}\right)\right]\sin(2\pi fx)$$

Analogous to the real Gabor filter, complex Gabor kernels at other angles can be obtained by rotating $g^c(x,y)$ over the range $[-\pi/2,\pi/2]$. The same design rules as described in Section 1.2.1 apply for the selection of the parameters σ_x, σ_y, and f.

The imaginary part of the complex Gabor filter approximates the Hilbert transform of the real Gabor filter; hence, the complex Gabor filter acts as a quadrature pair. Let $W_k^r(x,y)$ be the result of filtering a given image $I(x,y)$ with the real Gabor filter $g^r(x,y)$; let $W_k^i(x,y)$ be the result of filtering $I(x,y)$ with the imaginary component $g^i(x,y)$ of the complex Gabor filter; and let $W_k^c(x,y)$ be the result of filtering $I(x,y)$ with the complex Gabor filter $g^c(x,y)$. From Equation (2), it is evident that the following relationship holds: $|W_k^c(x,y)|^2 = |W_k^r(x,y)|^2 + |W_k^i(x,y)|^2$. The orientation field computed with the complex Gabor filter bank is given by the angle field $\phi^c(x,y)$, with

$$\phi^c(x,y) = \alpha_{k_{\max}} \text{ where } k_{\max} = \arg\{\max_k[|W_k^c(x,y)|]\},$$

and by the magnitude of the output of the complex Gabor filter at the optimal orientation $E^c(x,y) = |W_{k_{\max}}^c(x,y)|$.

1.3. Line operator

In a recent article, Zwiggelaar *et al.* [8] compared several methods for the detection of linear structures in mammographic images, namely: steerable filter [9], orientated bins [12], ridge detector [13], and line operator [4]. The line operator was shown to have the best detection performance among the oriented feature detectors investigated. The oriented feature detection methods investigated by Zwiggelaar *et al.* operate in a multiscale mode: the original image is decomposed in a Gaussian pyramid [14], and the methods are applied to each level of the pyramid.

The basic line operator kernel is sensitive to horizontal lines: detection of lines at an arbitrary orientation is achieved by rotating the basic line operator kernel. Let $H(x,y)$ be the average of N_L pixels along a horizontal line segment centered at (x,y), and $B(x,y)$ be the average of the

pixel values inside a square box of width N_L, centered at (x, y) and aligned with the Cartesian axes. The line operator kernel is then given by $L(x, y) = H(x, y) - B(x, y)$. In this work, we employ $N_L = 5$ pixels. Figure 1 illustrates the basic line operator kernel.
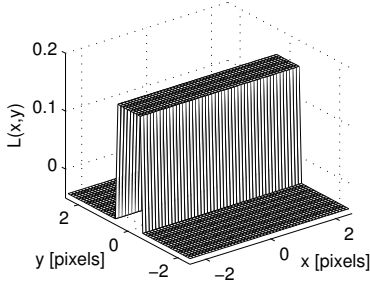

Figure 1. Basic line operator kernel, aligned with the x axis.

Let $I(x, y)$ be the image containing the lines to be detected, and $L_k(x, y)$ be the line operator kernel rotated to the angle $\beta_k = -\pi/2 + \pi k/18, k = 0, 1, \cdots, 17$. Let $W_k^l(x, y)$ be the result of filtering $I(x, y)$ with $L_k(x, y)$. The orientation of the line detected at pixel (x, y) is denoted by $\phi_l(x, y)$, and is obtained as

$$\phi^l(x, y) = \beta_{k_{max}} \text{ where } k_{max} = \arg\{\max_k[|W_k^l(x, y)|]\},$$

and the magnitude of the result of the line operator filtering is given by $E^l(x, y) = |W_{k_{max}}^l(x, y)|$.

Contrary to the steerable filters and the Gabor filters, the line operator does not provide a parameter for scaling. Multiscale analysis using the line detector is performed by decomposing $I(x, y)$ into a Gaussian pyramid [14], and applying the line operator at each level of the pyramid. Two operations are defined in the framework of Gaussian pyramids: reduction (low-pass filtering followed by decimation by a factor of two) and expansion (the image is augmented with the interleaving of zeros and subsequent filtering, expanding the resolution by a factor of two). The Gaussian pyramid of a given image $I(x, y)$ is a collection of images $I_p(x, y)$ obtained by the successive reductions, where p denotes the number of reductions applied. The expanded images $I_p^e(x, y)$ are obtained through the expansion of $I_p(x, y)$ to the original resolution of $I(x, y)$.

The scale of the line operator is defined as $\lambda = 2^p$, where p indicates that the line operator is applied to the reduced $I_p(x, y)$ image. The magnitude of the result of the line operator applied to $I_p(x, y)$ is expanded to the original resolution, in order to obtain the final magnitude $E^l(x, y)$. The line orientation produced by the application of the line detector to $I_p(x, y)$ is expanded to the original resolution using nearest-neighbor interpolation. (Linear interpolation is not applicable to angular quantities, as it would lead to inconsistent results. For instance, the average of 0° and 180° is 90°, indicating a vertical orientation that is incompatible with the horizontal orientations being averaged.)

2. Comparative analysis of the oriented feature detectors

The aim of the present work is to compare the detection performance and orientation accuracy of the five oriented feature detectors presented in Section 1. The detection performance is defined in terms of the ability of each filter to detect linear structures in the presence of noise and imprecision in the specification of scale. The orientation accuracy is given in terms of the cumulative angle error for the pixels belonging to the lines in the test pattern used.

A test image of size 512×512 pixels was employed in this work. The test pattern includes 34 line segments oriented at equally spaced angles, distributed radially around a circle with a radius of 70 pixels. Each line segment has a length of 115 pixels and a width of two pixels. The test image background was set to 0.4, and the line segments were set to 0.6, in the normalized scale $[0, 1]$ for gray levels. The test pattern was corrupted with various levels of Gaussian noise (standard deviation range: $[0, 0.5]$, in steps of 0.05), allowing the analysis of the robustness of each filter to noise. Figure 2a shows the test pattern corrupted by Gaussian noise of standard deviation 0.2.

The number of line segments was chosen as 34 in order to prevent synchronization between the angles of the kernels of the Gabor filter banks (real and complex) and in the line operator filter banks. Over the half-closed angular interval $[0, 180)$ degrees, we have 17 line segments and 18 kernels in each filter bank. As a consequence, the absolute angular error between the angle of a given line segment and the closest kernel angle in the filter bank will evenly span the range $[0, 5)$ degrees. The same reasoning applies to the line segments oriented at angles in the half-closed angular interval $[180, 360)$, because orientation angles follow a congruence arithmetic modulo 180 degrees.

The orientation field of the test image was obtained, for each level of noise, and for different values of the corresponding scale parameter with each filter. Figure 2 shows the orientation field magnitude obtained with each of the five oriented feature detectors.

For each filter, a pixel was considered to be part of a linear structure if the magnitude of the orientation field at that pixel exceeded a given threshold. In this manner, receiver operating characteristics (ROC) analysis [15] can be performed to investigate the detection performance of each filter. The detection performance measure was defined as
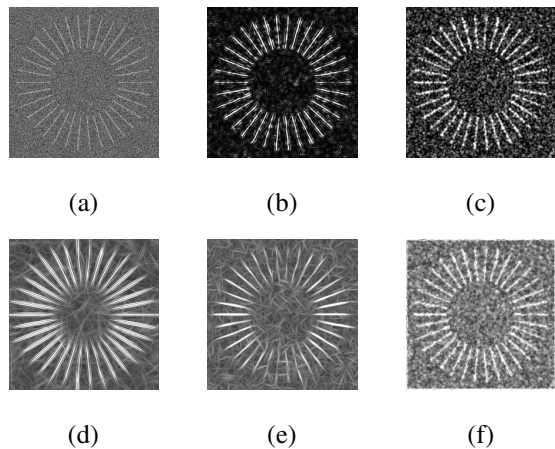
Figure 2. Orientation field magnitude obtained with each oriented feature detector. (a) Test pattern, corrupted with Gaussian noise (standard deviation $= 0.2$). (b) Steerable filter ($\sigma = 3.5$ pixels). (c) Quadrature steerable filter ($\sigma = 2.1$ pixels). (d) Real Gabor filter ($\tau = 10$ pixels). (e) Complex Gabor filter ($\tau = 5.5$ pixels). (f) Line operator ($\lambda = 2$ pixels).

Figure 3. Topographic map showing A_z for the oriented feature detectors studied, at various levels of noise and scale (std = standard deviation). (a) Steerable filter. (b) Quadrature steerable filter. (c) Real Gabor filter. (d) Complex Gabor filter. (e) Line operator.

the area under the ROC curve [15], denoted by A_z. The value of A_z was obtained for each noise level, and for several values of the scale parameter of each filter; the results are shown as topographic maps in Figure 3.

The definition of the scale parameter varies across the oriented feature detectors implemented in this work, introducing a degree of freedom in multiscale comparison of the different detectors: the scale measurement of each detector may differ from the remaining detectors by a multiplicative factor. Therefore, the base-ten logarithm of the scale parameter is employed in the present analysis, instead of the linear scale, in order to allow straightforward comparison of the different detectors. The logarithm operation converts any multiplicative factor into a summation constant, and comparisons of interval length in the scale parameter are not influenced by this constant. In particular, it is possible to integrate the detection performance of each detector (given by A_z, as previously mentioned) with respect to the logarithm of the scale parameter.

The following observations apply to all of the oriented feature detectors investigated in this work:

- The value of A_z decreases with the noise level. A slower decay in A_z versus noise denotes greater robustness to noise.

- For a given level of noise, there is an optimal range of values for the scale parameter associated with a high
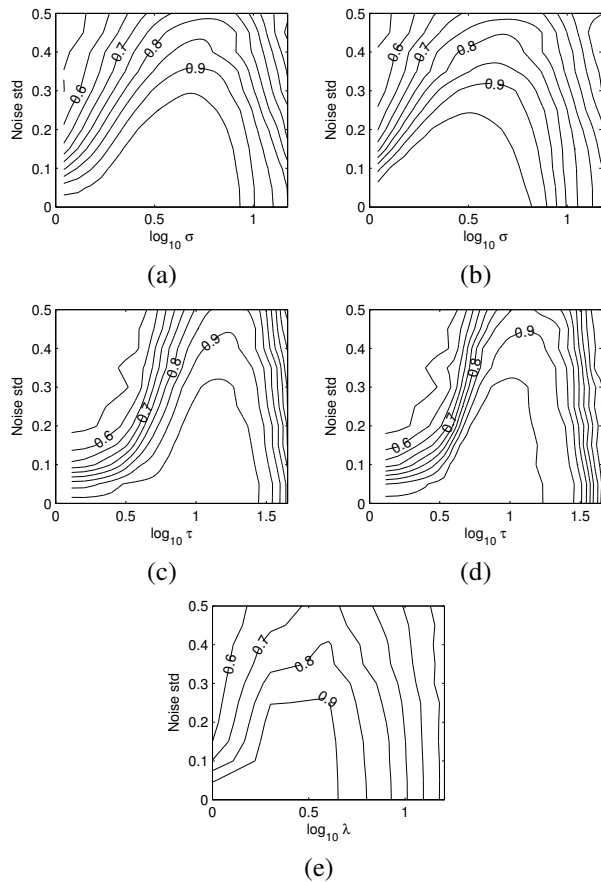
A_z value. This range can be interpreted as an indicator of robustness to imprecision in the specification of scale in the design of the filter, in relation to the actual width of the feature in the given image. Conversely, for a single-scale detector, the range of optimal values is associated with the variation of characteristic widths of oriented features for which the oriented feature detector can provide a high detection capability.

A measure to represent the combined robustness to noise and scale of each detector is proposed in this work, as the area of the domain (noise level, $\log_{10}$ of the scale parameter) for which $A_z > 0.9$. Table 1 presents the robustness measure of each detector.

In order to illustrate better the robustness of each oriented feature detector to imprecision in the specification of

scale, the standard deviation of the noise in the test image was set to 0.2, and the area under the ROC curve A_z was analyzed as a function of scale only, for each detector. The following parameters were obtained for each oriented feature detector, and the results are shown in Table 1:

- The best scale;

- The range of scale (in pixels) in which $A_z > 0.9$, called the detection range;

- The equivalent detection range, in millimeters, if the scale parameter is normalized around the width of 1 *mm* for the oriented feature.

In order to evaluate the angular precision of the detectors, the cumulative angular error was obtained at the best scale (shown in Table 1), and with a noise standard deviation of 0.2.; Figure 4 displays the results of the cumulative angular error analysis, i.e., the fraction of the positive (line) pixels whose angular error is smaller than a given angular tolerance. It is observed that the real and complex Gabor filters present the best accuracy: almost 100% of the line pixels (pixels belonging to the true line pattern in the test image) in the orientation field generated by these filters present an angular error smaller than 10 degrees.
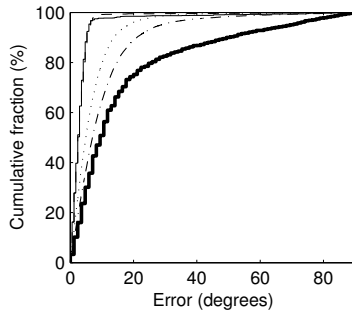

Figure 4. Cumulative error for each oriented feature detector: steerable filter (dotted line); quadrature steerable filter (dash-dot line); real Gabor filter (dashed line); complex Gabor filter (solid line); line operator (bold solid line). The curves associated with the real and complex Gabor filters overlap significantly.

3. Discussion

This work presented a performance analysis of five oriented feature detectors, in terms of their ability in the detection of oriented features and accuracy in the determination of the angle of the oriented features of interest. The performance measures were evaluated in the presence of noise and imprecision in the specification of scale.

All of the oriented feature detectors investigated in this work are based on filter banks consisting of filtering kernels that are sensitive to the presence of oriented features. Each filter presents a main positive lobe that is elongated at a certain orientation, surrounded by negative sidelobes that are parallel to the main lobe, in order to highlight the presence of linear features at a particular orientation. The results of filtering for each filter bank are combined to form two maps: the magnitude map, which indicates the intensity of the oriented feature at each pixel, and the angle map, which indicates the orientation of the feature at each pixel. The magnitude and angle maps are referred to as the orientation field of the image under analysis.

The detection performance of the oriented feature detectors in the presence of noise and scale imprecision is shown in Figure 3. It is observed that the all of the oriented feature detectors studied present a reduction in A_z with increasing noise, as expected. The Gabor filters (real and complex) are the most robust: the Gabor filters generally present a larger range of noise over which the detection performance is greater than 0.9. On the same token, the line operator is the most sensitive to noise. This result can be explained in terms of the spatial extent of the filters investigated: the main lobe of the Gabor filters has a larger length-to-width ratio than that of the other filters, thus enhancing more effectively the signal-to-noise ratio after filtering.

The robustness to imprecision in scale specification is also shown in Figure 3; it is noticed that, for a given level of noise in the test image, each oriented feature detector has an optimal range of scales in which the detector presents good detection performance (defined as $A_z > 0.9$). Table 1 shows the optimal scale range of each oriented feature detector, for a noise standard deviation level of 0.2 in the test image; conversion of the optimal scale range to millimeters is also given for easier comparison of the oriented feature detectors. The optimal scale range was converted to millimeters in such way that the oriented feature width of 1 *mm* is placed at the center of the optimal scale ranges. It is observed that the steerable filter, quadrature steerable filter, and the real and complex Gabor filters, present similar optimal scale range (in millimeters). The line operator has a significantly reduced optimal scale range (in millimeters), when compared to the other oriented feature detectors. It is possible that the implementation of scale control using the Gaussian pyramid results in reduced flexibility of the line operator to adapt to the size of the oriented feature to be detected.

It must be noted that the optimal scale range of all oriented feature detectors can be enhanced with the adoption of a multiscale strategy: each oriented feature detector can be applied to the image under analysis at different values of the scale parameter, resulting in an orientation field for each scale. The final orientation field is then obtained as follows:

Table 1. Robustness measure, best scale, and detection range for each oriented feature detector. The best scale and the detection range values are obtained at a noise standard deviation of 0.2 **in the test image.**

Detector	Robustness	Best scale [pixels]	Detection range [pixels]	Detection range [mm]
Steerable	0.25	3.5	$1.7 - 9.7$	$0.3 - 1.7$
Quadrature steerable	0.22	2.1	$1.3 - 7.3$	$0.3 - 1.7$
Real Gabor	0.33	10.0	$4.0 - 32.5$	$0.2 - 1.8$
Complex Gabor	0.34	5.5	$3.4 - 26.2$	$0.2 - 1.8$
Line operator	0.14	2.0	$1.9 - 4.3$	$0.6 - 1.4$

the magnitude of the final orientation field, at a given pixel, is the largest magnitude across the set of orientation fields that are obtained for each scale; the final angle is taken as the angle of the orientation field at the scale that provided the largest magnitude response. Nevertheless, the analysis of the optimal scale range is relevant: given a range of characteristic widths of several oriented features to be detected in an image, the analysis of the optimal scale range as above permits the appropriate selection of the scale parameter values, in the multiscale operation of each oriented feature detector. The set of scale parameter values must be chosen in such a manner that the union of the optimal scale ranges, associated with each scale chosen, covers the given range of the characteristic widths of the oriented features of interest.

The effect of noise and scale imprecision in the detection capability of each oriented feature detector may be summarized in a single combined robustness measure, as shown in Table 1 and described in Section 2. It can be observed that the real and complex Gabor filters have the best combined robustness measure, followed by the steerable filters; the line operator presents the lowest robustness. As mentioned in the preceding discussion, the Gabor and steerable filters have a similar optimal scale range, and the Gabor filters have a higher robustness to noise. The line operator has a reduced optimal scale range and low robustness to noise, when compared with the Gabor and steerable filters. Therefore, the ranking of the oriented feature detectors according to the combined robustness measure is consistent with the preceding discussion.

The angular precision of the oriented feature detectors is illustrated in Figure 4. It was observed that the Gabor filters have the best accuracy among the oriented feature detectors studied in this work. The line detector has the poorest orientation accuracy. These results are a consequence of the length-to-width aspect ratio of the main lobe of the filters. The Gabor filters have the highest aspect ratio; hence, the oriented Gabor kernel corresponding to the optimal orientation will prevail over the remaining kernels in the Gabor

filter bank in terms of the magnitude of the output, resulting in less ambiguity when deciding upon the orientation of the feature at a given pixel.

The steerable filter has the highest computational speed, because it depends on three filtering operations only, followed by the quadrature steerable filter, whose filter bank consists of seven filters. The line operator implemented in this work required 18 filters; the width of the filter kernels is small (5×5 pixels), allowing the efficient implementation of each line operator filter as a convolution operation. The Gabor filters require the highest computational effort: both the real and complex Gabor filter banks required 18 filters, which were implemented as frequency-domain filters instead of convolution operations in the space domain.

Combining the preceding observations, it can be noted that the Gabor filters present the best detection performance and angle accuracy, followed by the steerable filter, quadrature steerable filter, and the line operator. The steerable filter has the best computational performance, followed by the quadrature steerable filter; the Gabor filters have the highest computational requirement among the oriented feature detectors analyzed in this work. As a consequence, it is recommended that steerable filters be employed in applications where computational speed is important, and Gabor filters be used when high detection performance and angular accuracy are required. The Gabor filters are recommended in the case of noisy images or when the presence of oriented features is subtle. We have found the real Gabor filter to perform well in the detection of architectural distortion in mammograms [5, 6].

The line operator exhibited the poorest performance among the oriented feature detectors studied, in contrast with the results obtained by Zwiggelaar *et al.* [8]. This difference can be explained in terms of the methodological differences between the present work and that of Zwiggelaar *et al.* The key methodological aspects of the work of Zwiggelaar *et al.* (in regards to the evaluation of the detection performance of the line operator and the steerable filter) are as follows:

- The test image contained line segments of length 29 pixels; of width of two, four, and eight pixels; and of orientation from 0º to 180º in steps of 5º. The line segments were superimposed on a background image that consisted of a square region extracted from the mammographic image of a fatty breast. Artificial noise was not added to the test image.

- The oriented feature detectors studied were operated in a multiscale strategy as follows: the test image was decomposed into multiple scales using the Gaussian pyramid (four levels), and each oriented feature detector was applied to each level of the pyramid; the resulting orientation fields were combined to form the final orientation field for the given image. The scale of each oriented feature detector was kept constant; the scale of the image was changed in the Gaussian pyramid.

The Gaussian pyramid decomposition procedure effectively halves the resolution of the image from one level of the pyramid to the next. Therefore, the application of single-scale oriented feature detectors at each level of the pyramid is similar to the application of multiple-scale oriented feature detectors to the original image, where the values of the scale parameter follow a geometric progression of ratio two. Observe that the characteristic widths of the line segments used by Zwiggelaar *et al.* in the test image also follow this geometric progression pattern. Consequently, it is possible to associate each characteristic width of the line segments in the test image with a level in the Gaussian pyramid: in this manner, the performance evaluation of the multiple-scale oriented feature detectors shown in the work of Zwiggelaar *et al.* is analogous to a single-scale analysis of the oriented feature detectors, where the characteristic width of the test line segments is equal to two. Hence, the scale parameter in the steerable filter must be properly tuned in order to obtain the best detection performance from this filter, as shown in the present work. It is possible that the value of $\sigma = 0.8$ chosen by Zwiggelaar *et al.* for the steerable filter is suboptimal, resulting in a poorer performance when compared to the line operator.

A limitation of the present study is that only one basic test pattern was used (with variation in the noise level). Future work should include different patters that may reveal other aspects of the oriented feature detectors studied, and test the methods to the limits of their capability.

Acknowledgments

References

[1] N. Merlet and J. Zerubia. New prospects in line detection by dynamic programming. *IEEE Transactions on Pattern Analysis and Machine Intelligence*, 18(4):426–431, April 1996.

[2] E. R. Davies, M. Bateman, D. R. Mason, J. Chambers, and C. Ridgway. Design of efficient line segment detectors for cereal grain inspection. *Pattern Recognition Letters*, 24:413–428, 2003.

[3] S. Shah and P. S. Sastry. Fingerprint classification using a feedback-based line detector. *IEEE Transactions on Systems, Man, and Cybernetics - part B: Cybernetics*, 34(1):85–94, February 2004.

[4] R. N. Dixon and C. J. Taylor. Automated asbestos fibre counting. *Institute of Physics Conference Series*, 44:178–185, 1979.

[5] F. J. Ayres and R. M. Rangayyan. Characterization of architectural distortion in mammograms. *IEEE Engineering in Medicine and Biology Magazine*, pages 59–67, January 2005.

[6] F. J. Ayres and R. M. Rangayyan. Detection of architectural distortion in mammograms using phase portraits. In J. M. Fitzpatrick and M. Sonka, editors, *Proceedings of SPIE Medical Imaging 2004: Image Processing*, volume 5370, pages 587–597, San Diego, CA, February 2004.

[7] N. Karssemeijer and G. M. te Brake. Detection of stellate distortions in mammograms. *IEEE Transactions on Medical Imaging*, 15(5):611–619, 1996.

[8] R. Zwiggelaar, S. M. Astley, C. R. M. Boggis, and C. J. Taylor. Linear structures in mammographic images: Detection and classification. *IEEE Transactions on Medical Imaging*, 23(9):1077–1086, September 2004.

[9] W. T. Freeman and E. H. Adelson. The design and use of steerable filters. *IEEE Transactions on Pattern Analysis and Machine Intelligence*, 13(9):891–906, September 1991.

[10] C. K. Chui. *An Introduction to Wavelets*, volume 1 of *Wavelet Analysis and its Applications*. Academic Press, 1992.

[11] B. S. Manjunath and W. Y. Ma. Texture features for browsing and retrieval of image data. *IEEE Transactions on Pattern Analysis and Machine Intelligence*, 18(8):837–842, 1996.

[12] R. Zwiggelaar, T. C. Parr, and C. J. Taylor. Finding orientated line patterns in digital mammographic images. In *Proceedings of the 7th British Machine Vision Conference*, pages 715–724, Edinburgh, UK, 1996.

[13] T. Lindeberg. Edge detection and ridge detection with automatic scale selection. *International Journal of Computer Vision*, 30(2):117–154, 1998.

[14] P. J. Burt and E. H. Adelson. The Laplacian pyramid as a compact image code. *IEEE Transactions on Communications*, 31(4):532–540, April 1983.

[15] C. E. Metz. Basic principles of ROC analysis. *Seminars in Nuclear Medicine*, VIII(4):283–298, 1978.